The following publication Luo, D., Kyaw, A. K. K., Dai, T., Zhou, E., & Wong, W.-Y. (2024). Non-fused ring electron acceptors with an ethynylene linker for non-halogenated solvent-processed organic solar cells [10.1039/D4TC00721B]. Journal of Materials Chemistry C, 12(23), 8452-8460 is available at https://doi.org/10.1039/D4TC00721B.

Non-fused Ring Electron Acceptors with Ethynylene Linker for Non-Halogenated Solvent-Processed Organic Solar Cell

Dou Luo,[ab] Aung Ko Ko Kyaw,*[c] Tingting Dai,[d] Erjun Zhou,[d] and Wai-Yeung Wong*[ab]

[a] *Department of Applied Biology and Chemical Technology and Research Institute for Smart Energy, The Hong Kong Polytechnic University, Hung Hom, Hong Kong, PR China*

[b] *The Hong Kong Polytechnic University Shenzhen Research Institute, Shenzhen 518057, PR China*

[c] *Guangdong University Key Laboratory for Advanced Quantum Dot Displays and Lighting, Department of Electrical & Electronic Engineering, Southern University of Science and Technology, Shenzhen 518055, China.*

[d] *National Center for Nanoscience and Technology, Beijing 100190, China*

* Corresponding author, E-mail address: aung@sustech.edu.cn (Prof. A. K. K. Kyaw); wai-yeung.wong@polyu.edu.hk (Prof. W.-Y. Wong)

Abstract

This study explores the design, synthesis and application of two non-fused ring electron acceptors (NFREAs), namely PAcT-Cl and CAcT-Cl, featuring an ethynylene linker, in non-halogenated solvent-processed organic solar cells (OSCs). The introduction of the ethynylene linker is found to effectively regulate the energy levels and molecular conformations of the acceptors. PAcT-Cl, with an alkoxy phenyl group core, exhibits downshifted highest occupied molecular orbital energy levels, higher electron mobility, and enhanced molecular packing order in neat thin films compared to CAcT-Cl, which incorporates a 4H-cyclopenta[1,2-b:5,4-b’]dithiophene core. As a result, the J52:PAcT-Cl device processed with *o*-xylene achieves a power conversion efficiency (PCE) of 10.22%, attributed to efficient charge transport and improved crystallinity, outperforming the OSC based on CAcT-Cl with inferior crystallinity (PCE =7.32%). Furthermore, this study investigates the performance of PAcT-Cl-based devices processed with different solvents. Overall, this work demonstrates the application of ethynylene linker in efficient NFREAs and discloses the potential of non-halogenated solvents for preparing NFREAs-based devices.

Keywords: ethynylene bridges, non-halogenated solvent, non-fused ring electron acceptor, organic solar cell

1. Introduction

In recent years, organic solar cells (OSCs), composed of a wide-bandgap polymer donor and near-infrared absorption fused-ring electron acceptors (FREAs), have drawn tremendous attention due to their unique advantages such as mechanical flexibility, semi-transparency and cost effectiveness.[1-4] To date, the power conversion efficiencies (PCEs) of single-junction OSCs have exceeded 19% because of the ingenious design and synthesis of non-fullerene acceptors (NFAs),[5-13] hinting at the possibility of exceeding 20% PCE in the near future through advancements in material designs, device engineering and device physics. However, despite the rapid progress in FREAs, inherent drawbacks such as complex synthesis routes, low yields and high costs, make the large-scale applications murky.[14-17] Taking this into consideration, non-fused ring electron acceptors (NFREAs) have emerged, with devices based on NFREAs achieving PCEs exceeding 17%, showing great potential compared to FREAs.[18-23] Our group has synthesized numerous NFREAs, employing diverse molecular design strategies. For example, by introducing electron-deficient diketone units into the central core, we synthesized NFREA TPDC-4F, exhibiting a deep highest occupied molecular orbital (HOMO) and achieving a device PCE exceeding 13.5% with an open-circuit voltage (V_{oc}) exceeding 0.85 V.[24] Besides, by optimizing the alkyl side chains and end groups, we developed a new NFREA C8C8-4Cl, achieving a PCE exceeding 14%.[25,26] Very recently, we adopted a ternary strategy to push the PCE over 16%.[27] These reports indicate that the PCEs based on NFREAs can be further enhanced through innovative molecular design approaches.

Apart from the molecular design, state-of-the-art OSCs typically reply on halogenated solvent systems, such as chloroform (CF), 1,2-dichlorobenzene (*o*-DCB) and chlorobenzene (CB), to achieve optimal performance.[5,7,28-30] However, the use of these halogenated solvents poses inherent risk to human health and environment, hindering the future large-scale production of OSCs. On the other hand, non-halogenated solvents offer potential alternatives, yet controlling the crystallization and film forming process when utilizing them but related research remains challenging. This is primarily due to the influence of non-halogenated solvents with different boiling points, solubility parameters, and saturation vapor pressure on factors such as phase separation, molecular stacking, domain size, and purity in the active layers. Consequently, optimizing the morphology of NFREA-based devices using non-halogenated solvents remains a significant challenge.

Keeping these in mind, we designed and synthesized two new NFREAs, namely PAcT-Cl and CAcT-Cl, to dedicatedly process them in non-halogenated solvents. PAcT-Cl features an alkoxy phenyl central core, which has been widely used as core in many high-performance NFREAs for regulating the molecular planarity, absorption, and energy levels,[27] while CAcT-Cl incorporates a 4H-cyclopenta[1,2-b:5,4-b']dithiophene (CPDT) central core, which is seldom used as central core before. Both acceptors linked to a CPDT bridge by an ethynyl linker. The rationale behind our design includes several key factors: (1) CPDT bridge is widely used due to its extended conjugation and ease of modification on the sp^3 carbon atoms;[14] (2) ethynylene linker with electron-withdrawing nature can lower the HOMO energy levels of the acceptors to align with high performance deep HOMO polymer donors; (3) ethynylene linker exhibits cylinder-like π-electron density, enhancing intermolecular π–π stacking and facilitating intermolecular charge transport; (4) rigid acetylene linkages promote planar conformations for the acceptors to enhance the electron mobility; (5) PAcT-Cl and CAcT-Cl were synthesized via Sonogashira coupling reactions, avoiding toxic stannyl intermediates and lithiation reactions. Surprisingly, compared to CAcT-Cl, PAcT-Cl with an alkoxy phenyl group in the central core exhibited a deeper HOMO level of –5.61 eV (HOMO level of –5.35 eV for CAcT-Cl). Moreover, PAcT-Cl exhibited higher electron mobility, and preferable face-on orientation in the neat thin film. As a result of these advantages, the best-performing devices based on J52:PAcT-Cl and J52:CAcT-Cl afforded PCEs of 10.22% and 7.32%, respectively, using non-halogenated *o*-xylene as the processing solvent. We also investigated the performance of the devices fabricated using CF, *o*-DCB and CB solvents. The superior performance of PAcT-Cl-based device can be attributed to efficient charge transport (separation) and improved crystallinity. Overall, our work indicates that employing ethynylene linker to construct NFREAs is a promising strategy for achieving high-performance and low-cost OSCs, and we also reveal the potential of non-halogenated solvent in preparing NFREAs-based devices.

2. Results and Discussion

Synthesis and characterization of acceptors

The chemical structures of PAcT-Cl, CAcT-Cl and J52 are shown in Fig. 1a, while detailed synthetic procedures for the acceptors are provided in Scheme S1. All synthesis steps involve commonly used reaction with high yields, significantly reducing the synthesis complexity. Specially, the synthesis of acetylene linkages commonly used Sonogashira coupling, avoiding highly toxic reagent. We employed various characterizations, including ^{1}HNMR, ^{13}C NMR, high-resolution mass spectroscopy (HRMS), and microanalysis, to confirm the high purity of the molecules. Next, we investigated the molecular electrostatic potential (ESP) distribution as well as molecular geometry by conducting density functional theory (DFT) calculations. In order to accelerate the calculation, the alkyl chains were replaced with methyl groups. As shown in Fig. S1a, the CPDT π-bridge exhibits a positive ESP value, while O-atoms and cyano group exhibit negative values. For CAcT-Cl, the central unit of CPDT group exhibits a substantial positive ESP value, indicating the different electron cloud distribution compared with PAcT-Cl (Fig. S1b). Different ESP distributions in PAcT-Cl and CAcT-Cl play a critical role in affecting the inter- and intrachain electronic coupling, which will affect the optical response and molecular stacking. What's more, it has been confirmed that the BDT-based polymer donors exhibited strong electronegativity along the conjugated main chains.[31] The strong electropositivity of the CPDT units in the PAcT-Cl and CAcT-Cl will potentially interact with the conjugated main chains of J52 donor and influence their molecular organization during the film-formation process. The HOMO/LUMO levels of PAcT-Cl and CAcT-Cl were then calculated to be –5.50/–3.63 eV and –5.36/–3.68 eV, respectively (Fig. S1c-d). What's more, the optimized configuration of the acceptors shows a complete planar molecular architecture, which is attributed to the rigid acetylene linkages. The planar structure is conductive to enhance the intermolecular π–π stacking and contribute to the charge transfer (Fig. S1e-f).

Optical and electrochemical properties

The absorption spectra of PAcT-Cl and CAcT-Cl in dilute chloroform solutions and neat films are shown in Fig. 1b and 1c, with their optical data summarized in Table 1. The maximum absorption peak of PAcT-Cl is located at 687 nm, and this peak is red-shifted to 707 nm for CAcT-Cl. The redshifted spectral band in dilute solution for CAcT-Cl indicates that the central CPDT unit of CAcT-Cl enhances the intramolecular charge transfer (ICT) in the molecule. Besides, a larger full width at half maximum (FWHM) for CAcT-Cl was observed compared with PAcT-Cl. As has been reported in the literature reports, improving the electron-donating property or extending the π-conjugation in the central core will enhance the ICT effect and then contribute to the broader absorption in the solution state.[32,33] The central core of CPDT unit for CAcT-Cl exhibited stronger electron-donating and more extended π-conjugation than that of PAcT-Cl with alkoxy phenyl group, resulting in improved ICT in the related molecule. This is probably due to the more efficient intramolecular charge transfer from electron rich core unit (D) to electron-deficient end groups (A). As discussed in the ESP analysis, the central unit of CAcT-Cl exhibits a stronger positive ESP value than that of PAcT-Cl, facilitating intramolecular charge transfer. In the solid state, the maximum absorption peaks of PAcT-Cl and CAcT-Cl are centered at 756 and 716 nm, with the same trend of larger FWHM for CAcT-Cl. The absorption onsets of the films occur at ~824 and ~876 nm for PAcT-Cl and CAcT-Cl, respectively, yielding optical bandgaps (E_g) calculated at 1.50 and 1.41 eV, respectively, using the empirical formula $E_g = 1240/\lambda_{onset}$. Additionally, the absorption spectrum of polymer donor J52 is shown in Fig. 1c. Notably, both PAcT-Cl and CAcT-Cl exhibit complementary absorption bands with J52, promoting photon utilization and contributing to the J_{sc} of the device.

The electrochemical properties of the acceptors were measured by cyclic voltammetry (CV), as depicted in Fig. S2. From the CV analysis, the HOMO/LUMO levels for PAcT-Cl and CAcT-Cl were calculated to be –5.61/–3.59 eV and –5.35/–3.61 eV, respectively. As shown in Fig. 1d, the energy levels of the acceptors matched well with the J52, indicating efficient charge transfer between the polymer donor and acceptors. The HOMO level for CAcT-Cl was deeper than that of FG6 (HOMO of –5.29 eV), which contains the same molecular structure but with an ethylene linkage, indicating that ethynylene linker with electron-withdrawing nature can lower the HOMO energy level.[34] Besides, the electron-transport characteristics of the pure films of PAcT-Cl and CAcT-Cl were investigated by the space-charge-limited current (SCLC) method in the electron-only device (ITO/ZnO/active layer/PDINN/Ag). The electron mobility curves of the acceptors are given in Fig. S3, with detailed data summarized in Table 1. The pristine PAcT-Cl film exhibited an electron mobility (μ_e) value of 1.08 × 10^{-4} $cm^2\ V^{-1}\ s^{-1}$, higher than that of CAcT-Cl (8.5 × 10^{-5} $cm^2\ V^{-1}\ s^{-1}$). Generally, the electron mobilities of pure films correlate well with crystallinity and molecular stacking. Here, the higher electron mobility of PAcT-Cl suggests preferable π–π stacking and crystallinity compared to CAcT-Cl, which will be discussed in the following sections.

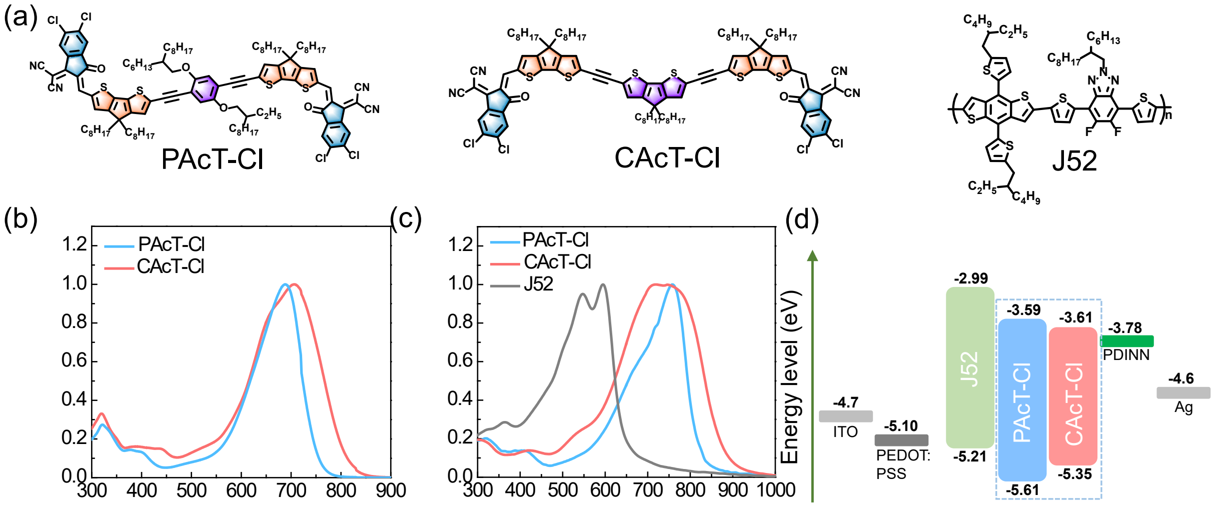

Fig. 1 (a) The chemical structures of PAcT-Cl, CAcT-Cl and J52. UV–vis absorption spectra of neat PAcT-Cl, CAcT-Cl in (b) dilute chloroform solution and (c) as cast films. (d) The energy levels of donor and acceptors.

Table 1 Optical, electrochemical, and electron mobility properties of PAcT-Cl and CAcT-Cl.

Material	λ_{max} a) (nm)	λ_{max} b) (nm)	λ_{onset} b) (nm)	E_g^{opt} c) (eV)	HOMO d) (eV)	LUMO d) (eV)	Mobility e) ($cm^2\ V^{-1}\ s^{-1}$)
PAcT-Cl	687	756	824	1.50	−5.61	−3.59	1.08 × 10^{-4}
CAcT-Cl	707	749	876	1.41	−5.35	−3.61	8.5 × 10^{-5}

a) In chloroform solution. b) In a neat film. c) Calculated from the onset of the absorption spectrum of the film. $E_g^{opt} = 1240/\lambda_{onset}$. d) Evaluated by CV measurements. e) Tested by SCLC model.

Photovoltaic properties

We fabricated corresponding devices, using the conventional structure of ITO/PEDOT:PSS/J52:acceptors/PDINN/Ag and non-halogenated *o*-xylene as solvent for polymer donor and acceptors, to investigate the photovoltaic properties. All fabricated cells were tested under simulated AM1.5G illumination at an intensity of 100 mW cm^{-2}. The optimal current density (J)–voltage (V) curves of the best-performing devices are shown in Fig. 2a and their corresponding photovoltaic parameters are summarized in Table 2. The J52:PAcT-Cl-based devices achieved a maximum PCE of 10.22% with V_{oc} of 0.784 V, a J_{sc} of 21.00 mA cm^{-2}, and a FF of 62.1%. For the CAcT-Cl-based devices, a lower V_{oc} of 0.724 V and an inferior PCE of 7.32% were obtained, with a J_{sc} of 20.14 mA cm^{-2} and FF of 50.3%. The decreased V_{oc} of CAcT-Cl-based devices is reasonable, considering the downshifted LUMO energy levels. Except for similar J_{sc} values for both devices, the PAcT-Cl-based devices exhibited a higher FF than that of PAcT-Cl-based devices, which can be attributed to the less charge recombination and better molecular stacking morphology (vide infra). Furthermore, we prepared devices using common halogenated solvents such as CF, CB and *o*-DCB. The best-performing devices from eight devices and detailed data are shown in Fig. S4 and Table S1. When CF was used as the processing solvent, both PAcT-Cl- and CAcT-Cl-based devices showed decreased V_{oc}, J_{sc} and FF, resulting in the lower PCEs 8.65% and 5.81%, respectively. The poor performance of CF-processed devices may be attributed to the unfavorable morphology. Additionally, another two high boiling point solvents, CB and *o*-DCB, were also used to prepare devices. Unfortunately, compared with *o*-xylene, the PCEs of CB- and *o*-DCB-processed devices were still not enhanced. These results indicated that the crystallization process and morphology of the devices can be largely regulated by using high boiling point green solvent of *o*-xylene. However, further investigation is needed to understand the underlying morphology regulation. External quantum efficiency (EQE) curves were investigated to verify the J_{sc} values of the devices processed with *o*-xylene (Fig. 2b). Distinct prominent EQE response ranges of 400–450nm, 550-650 nm and 750-850 nm were observed for PAcT-Cl-based devices, with a maximum peak value exceeding 80% at 769 nm. CAcT-Cl-based devices showed a broader EQE response than PAcT-Cl-based devices, with a maximum peak value exceeding 78% at 588 nm. This is consistent with the UV-vis absorption spectra of the blend films (Fig. S5). However, both the EQE curves of PAcT-Cl- and CAcT-Cl-based devices exhibited uneven response, potentially accounting for the lower J_{sc} in the devices. The integrated J_{sc} values calculated from the EQE curves of the PAcT-Cl and CAcT-Cl based devices are 20.1 and 20.0 mA cm^{-2}, respectively, consistent with the J_{sc} values from the J–V curves.

Charge collection, recombination, and transport

The charge collection probability (P_c) of the non-halogenated solvent-processed devices was investigated by plotting photocurrent (J_{ph}) versus effective voltage (V_{eff}).[35] P_c, determined from J_{ph}/J_{sat}, where J_{sat} is the saturated J_{ph}, yielded the values of 0.906 and 0.876 for PAcT-Cl- and CAcT-Cl-based devices, respectively, indicating more efficient charge collection in the PAcT-Cl-based devices. Besides, the power law relationship between J_{sc} and input power of light intensity (P_{in}), described as $J_{sc} \propto P_{in}^{\alpha}$, was employed to explore the charge recombination properties.[36] As shown in Fig. 2d, the α values of devices based on J52:PAcT-Cl and J52:CAcT-Cl are 0.925 and 0.862, respectively, indicating less bimolecular recombination occurred in the former device. The dependence of V_{oc} on the P_{in}, described as $V_{oc} \propto nk_BT/q\ \ln(P_{in})$, where k_B, T, and q represent the Boltzmann constant, temperature in Kelvin, and elementary charge, respectively, was evaluated to study the trap-assisted recombination.[37] As shown in Fig. 2e, the n values of J52:PAcT-Cl and J52:CAcT-Cl devices are 1.22 and 1.42, respectively, indicating a lower trap-assisted recombination in the PAcT-Cl-based devices compared to CAcT-Cl-based devices. Additionally, the dark current curves are shown in Fig. S6, where the J52:PAcT-Cl devices exhibited lower leakage current compared to the J52:CAcT-Cl devices, confirming less recombination in the devices. To further study the charge trap in the two blend films, we measured the trap density of J52:PAcT-Cl and J52:CAcT-Cl devices using SCLC method (Fig. 2f). The total trap density in the blend can be calculated using the formula: $V_{TFL}=(qN_tL^2)/(2\varepsilon_0\varepsilon)$, where V_{TFL} is the trap-filled limit voltage, q is the elementary charge, N_t is the total trap density, L is film thickness, ε_0 and ε are permittivity of free space and relative permittivity of the material, respectively.[38] The total N_t of J52:PAcT-Cl was calculated to be 1.05×10^{16} cm^{-3}, lower than that of J52:CAcT-Cl device (2.18×10^{16} cm^{-3}). The lower trap density in the J52:PAcT-Cl blend film suppressed charge recombination in the devices.

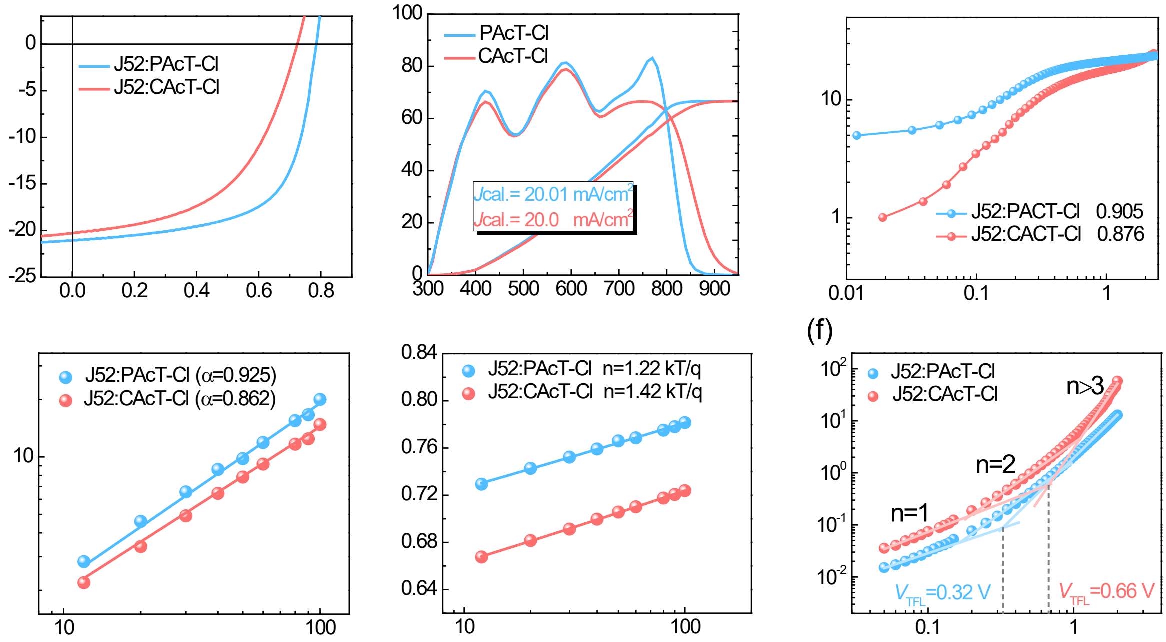

Fig. 2 (a) *J–V* characteristics of the OSCs based on *o*-xylene-processed J52:PAcT-Cl, J52:CAcT-Cl under AM1.5G illumination (100 mW cm^{-2}). (b) The corresponding EQE spectra of J52:PAcT-Cl and J52:CAcT-Cl. (c) J_{ph} versus V_{eff} curves. (d) Light intensity dependence of J_{sc}. (e) Light intensity dependence of V_{oc}. (f) *J–V* characteristics of electron-only devices based on J52:PAcT-Cl and J52:CAcT-Cl (n represents the slope of the fitting line).

Table 2 Photovoltaic parameters of OSCs based on J52:PAcT-Cl and J52:CAcT-Cl.

Active layer	V_{oc} (V)	J_{sc} (mA cm^{-2})	J_{sc} (mA cm^{-2})$^{a)}$	*FF* (%)	*PCE* (%)$^{b)}$
J52:PAcT-Cl	0.784 (0.78±0.004)	21.00 (20.5±0.5)	20.01	62.1 (61.0±1.1)	10.22 (10.0±0.22)
J52:CAcT-Cl	0.724 (0.72±0.004)	20.14 (19.3±0.84)	20.0	50.3 (49.1±1.2)	7.32 (7.02±0.3)

$^{a)}$ Calculated current densities from EQE curves. $^{b)}$ Average PCEs from ten devices.

The charge extraction capability of non-halogenated solvent-processed OSCs was assessed by the transient photocurrent (TPC) curves.[39] As shown in Fig. 3a, the charge extraction times were 0.54 μs and 1.03 μs for J52:PAcT-Cl and J52:CAcT-Cl devices, respectively. Notably, the

J52:PAcT-Cl device demonstrated a shorter photocurrent decay time compared to that of J52:CAcT-Cl, indicating a faster charge extraction capability and suppressed monomolecular recombination. Besides, transient photovoltage (TPV) measurement was used to evaluate the charge carrier lifetimes and the degree of charge recombination.[26] The carrier lifetimes of the J52:PAcT-Cl and J52:CAcT-Cl devices were 9.34 μs and 7.00 μs, respectively (Fig. 3b). Obviously, the longer carrier lifetime of the device will induce less recombination and better charge transport. This result was consistent with the results of $J_{\mathrm{sc}} \propto P_{\mathrm{in}}^{\alpha}$ and the dark current test. Furthermore, photo-CELIV was employ to quantify charge carrier mobility (μ) using the formula, $\mu = 2d^2/[3At_{\mathrm{max}}^2(1 + 0.36\Delta j/j(0))]$, where d is the active layer thickness, A is the voltage ramp, t_{max} is the maximum current time, Δj is the peak transient current, and $j(0)$ is the displacement current (Fig. 3c).[40] The calculated parameters are summarized in Table 3. The μ values were determined as 3.58×10^{-5} cm^2 V^{-1} s^{-1} and 2.74×10^{-5} cm^2 V^{-1} s^{-1} for J52:PAcT-Cl and J52:CAcT-Cl devices, respectively. The higher charge carrier mobility observed in PAcT-Cl-based device confirms better charge transport. Furthermore, the hole and electron mobilities of the blend films were studied by SCLC tests. As shown in Fig 3d and Fig. S7, the μ_{h} and μ_{e} were estimated to be 7.83×10^{-5} and 6.39×10^{-5} cm^2 V^{-1} s^{-1} for the J52:PAcT-Cl blend film, respectively, resulting in a $\mu_{\mathrm{h}}/\mu_{\mathrm{e}}$ ratio of 1.22. In comparison, the J52:CAcT-Cl blend film showed a lower μ_{h} of 3.11×10^{-5} cm^2 V^{-1} s^{-1} and μ_{e} of 1.96×10^{-5} cm^2 V^{-1} s^{-1}, giving a larger $\mu_{\mathrm{h}}/\mu_{\mathrm{e}}$ of 1.58 (Table S2). The higher carrier mobility and more balanced $\mu_{\mathrm{h}}/\mu_{\mathrm{e}}$ ratio of the J52:PAcT-Cl device contributed to increased FF compared to J52:CAcT-Cl.

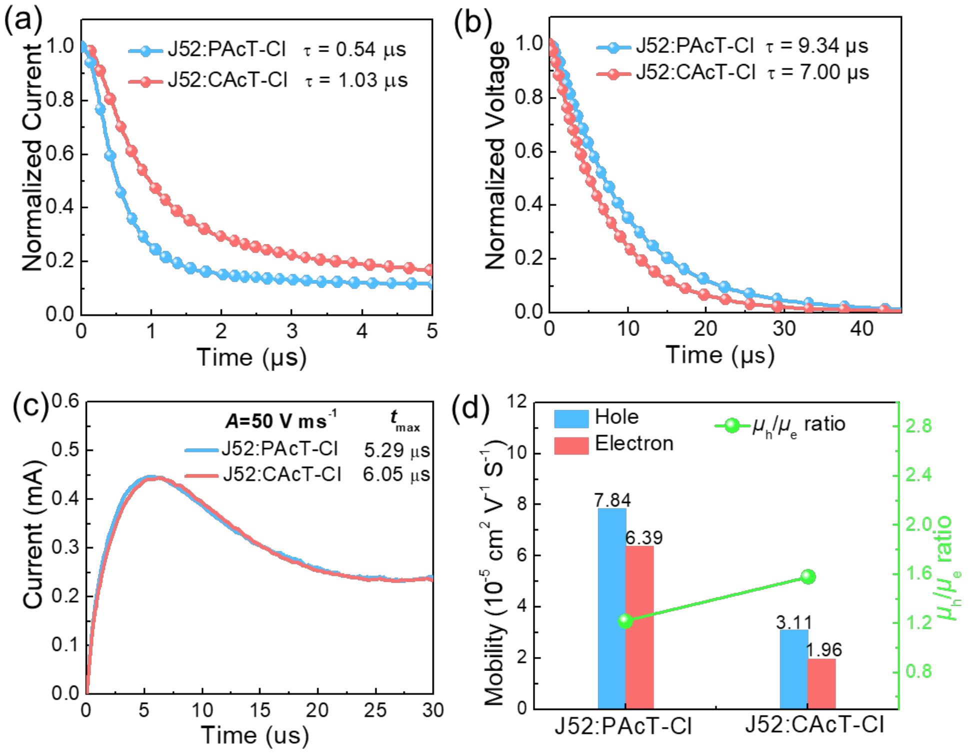

Fig. 3 (a) TPC and (b) TPV measurements of the photovoltaic devices. (c) Photo-CELIV plots with a voltage ramp of 50 V ms^{-1}. (d) The hole and electron mobilities and μ_h/μ_e ratio based on the J52:PAcT-Cl and J52:CAcT-Cl.

Table 3 The parameters extracted from photo-CELIV.

Active layer	A (V ms^{-1})	t_{max} (μs)	Δj (mA)	j (0)	$\Delta j/j(0)$	d (nm)	μ (cm^2 V^{-1} s^{-1})
J52:PAcT-Cl	50	5.29	0.213	0.233	0.914	100	3.58×10^{-5}
J52:CAcT-Cl	50	6.05	0.210	0.233	0.901	100	2.74×10^{-5}

To investigate the charge transfer dynamics in the respective devices, transient absorption spectroscopy (TAS) measurements were conducted. A 500 nm laser was first used to excite the blend films and study electron transfer.[41,42] As shown in Fig. 4a, 4b, the negative signals in the range of 500–610 nm and 700–830 nm are assigned to the ground state bleaching (GSB) signals of J52 and acceptors, respectively. Besides, we also found two positive signals at around 630 nm and 860 nm both for J52:PAcT-Cl and J52:CAcT-Cl, respectively, indicating the excited state absorption (ESA) signals. Then the electron transfer properties are assessed by fitting the decay kinetics curves and obtaining the fast component (τ_1) and slow component (τ_2) (Fig. 4e). τ_1

represents ultrafast exciton dissociation at the donor–acceptor interface, while τ_2 evaluates the diffusion of excitons in the donor phase towards the interface before dissociation. The J52:PAcT-Cl and J52:CAcT-Cl films exhibited average carrier lifetime of 97.76 and 125.35 ps, respectively. It should be noted that both τ_2 values for J52:PAcT-Cl and J52:CAcT-Cl films are excessively large, resulting in a considerable electron transfer time for both blend films (Table S3). Overall, the shorter carrier lifetime of J52:PAcT-Cl film indicates a faster electron transfer rate compared to J52:CAcT-Cl film, which contributes to balanced charge transfer and enhanced FF. Additionally, we employed an 800 nm excitation wavelength to study the hole-transfer processes in the blend films. The TA images and corresponding spectra with various decay times are presented in Fig. S8. As the GSB signals at 770 nm decay, donor GSB signals at 600 nm gradually emerge in the blend films, indicating hole transfer from the acceptors to the donor.[26] Then the hole transfer processes were verified by the decay dynamics of the 600 nm GSB signals of J52 (Fig. S9). We found that the intensity of hole transfer rate for J52:PAcT-Cl was stronger than that of J52:CAcT-Cl at the initial timescale of ≈10 ps, implying the faster hole transfer.

The charge transfer was further investigated using steady-state photoluminescence (PL) emission spectra of thin-film PAcT-Cl, CAcT-Cl and their blend films with J52, analyzing the quenching efficiency. As shown in Fig. 4g and 4h, the PL intensities of both PAcT-Cl and CAcT-Cl were significantly quenched in the J52:PAcT-Cl and J52:CAcT-Cl blend films, with quenching efficiency of 92% and 88.1%, respectively, indicating efficient charge transfer from the acceptors to the donor. The higher PL quenching efficiency observed for J52:PAcT-Cl suggests enhanced charge transfer, consistent with the results obtained from TA tests.

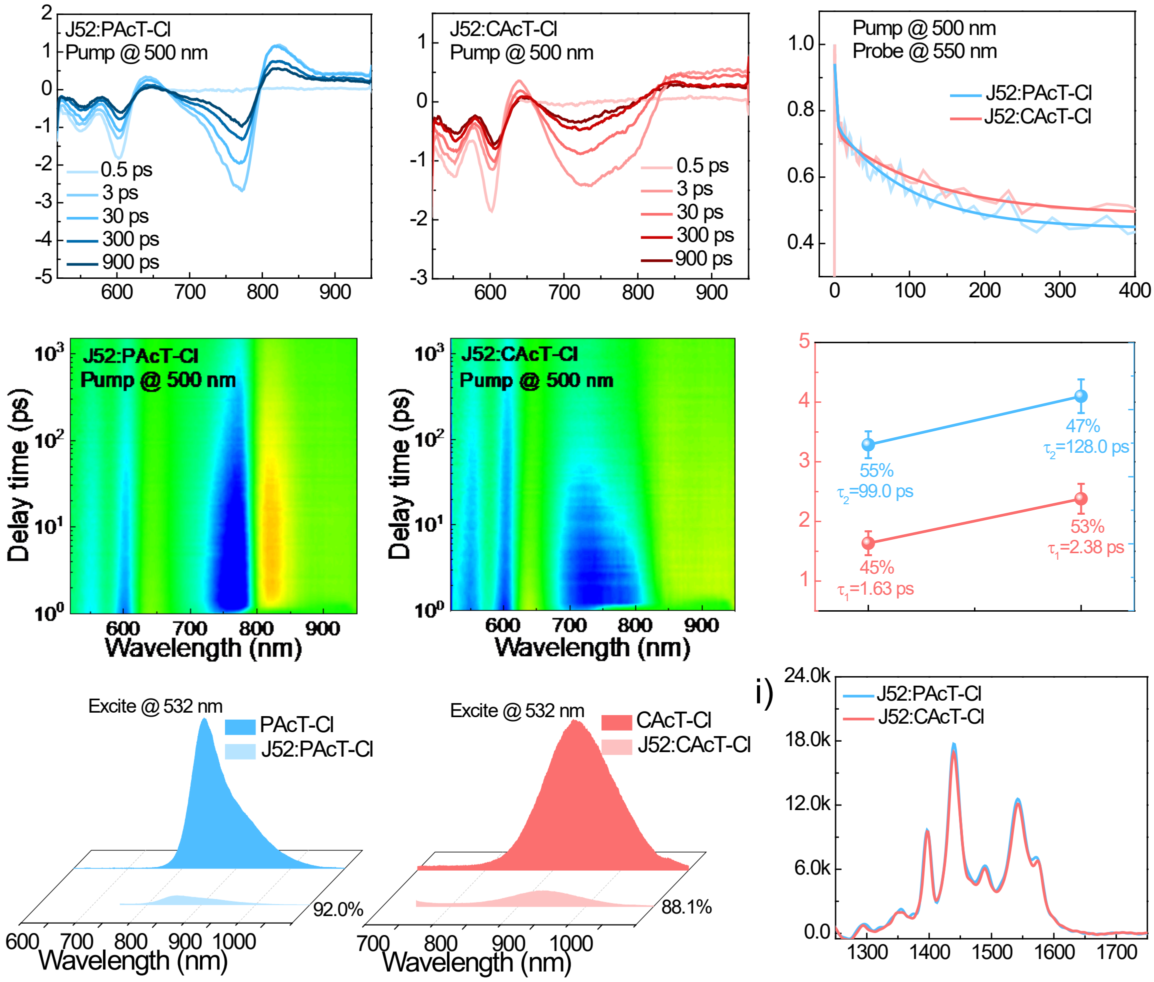

Fig. 4 Representative TA spectra of (a) J52:PAcT-Cl and (c) J52:CAcT-Cl blend films under 500 nm excitation. The corresponding color plot of TA spectra of (b) J52:PAcT-Cl and (d) J52:CAcT-Cl. (e) The decay traces of GSB at 550 nm for the blend films with an excitation wavelength of 500 nm. (f) Comparisons of τ_1 and τ_2 of different blends. PL spectra of (g) PAcT-Cl, J52:PAcT-Cl and (h) CAcT-Cl, J52:CAcT-Cl blend films under 532 nm light excitation. (i) Raman spectra of J52:PAcT-Cl and J52:CAcT-Cl blend films.

Blend film morphology

The morphology of the active layer plays an important role in the device performance. Raman spectroscopy tests were first conducted to study the molecular stacking in the blend films. As shown in Fig. 4i, the Raman spectra of J52:PAcT-Cl and J52:CAcT-Cl blend films are very similar because of the similar molecular structures of PAcT-Cl and CAcT-Cl. The Raman bands at ~1397–1440 cm^{-1} and 1543 cm^{-1} were identified as the v(C-C) and v(C=C) vibrations of the fused thiophene ring in the cyclopentadithiophene (CPDT) unit and the ring stretch of the central units, respectively. The Raman intensity of J52:PAcT-Cl between 1350 cm^{-1} and 1550 cm^{-1} is stronger than that of J52:CAcT-Cl, implying better molecular stacking in the blend film. Besides, the J52:PAcT-Cl film exhibited a smaller full width at half maxima (FWHM) compared to that of J52:CAcT-Cl film, indicating an increase in the molecular order and packing along the entire backbone (Fig. S10).[41] The miscibility and compatibility between the J52 and acceptors were evaluated by determining the surface energy of the films. The contact angles of water and diiodomethane droplets on the pure films are presented in Fig. S11. The interaction parameter χ, calculated as $\chi = k(\sqrt{\gamma_A} - \sqrt{\gamma_B})^2$, where k is a positive constant, and γ_A and γ_B refer to the surface tension of A and B in its neat films, respectively,[43,44] was used to assess the miscibility. The calculated χ is found to be $\chi_{J52/PAcT\text{-}Cl} = 0.117$ K, $\chi_{J52/CAcT\text{-}Cl} = 0.434$ K, indicating favourable miscibility between J52 and PAcT-Cl (Table S4). The enhanced miscibility will promote the formation of a well-mixed donor/acceptor phase in the blends. Usually a suitable donor/acceptor phase can contribute to the preferable morphology.

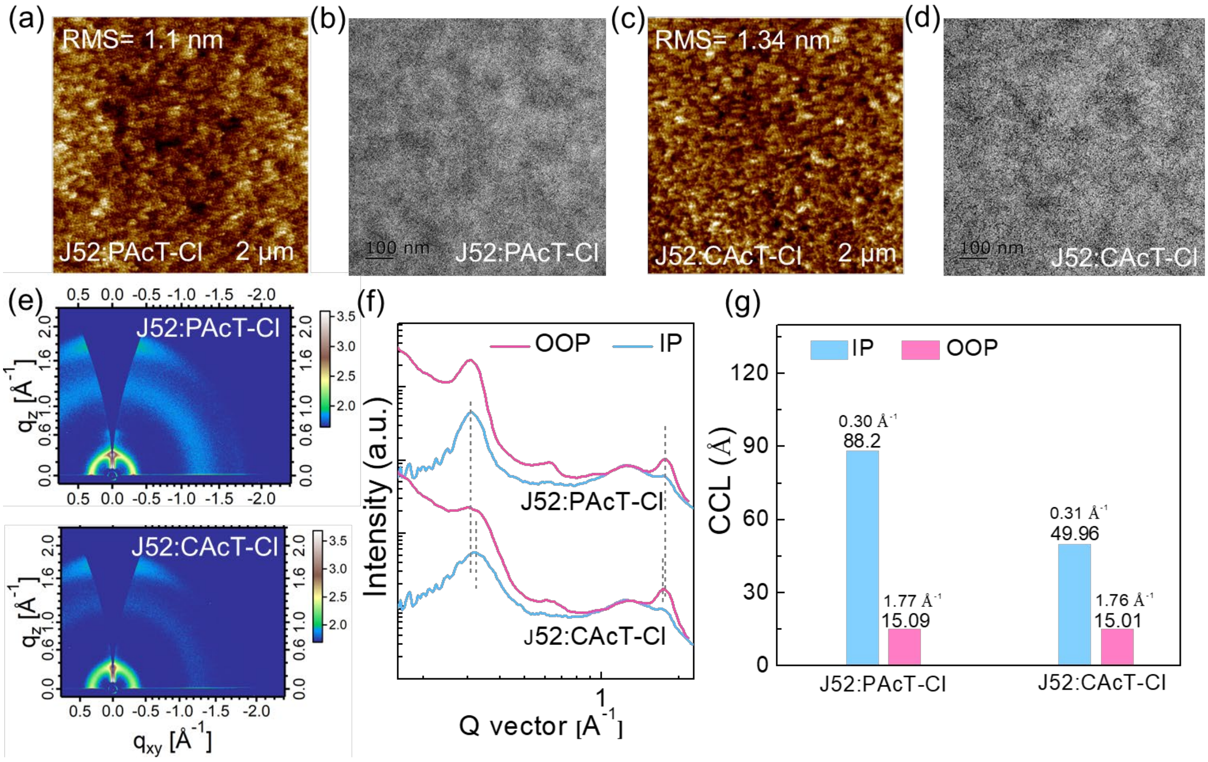

Fig. 5 Tapping-mode AFM height image of (a) J52:PAcT-Cl and (c) J52:CAcT-Cl films. TEM image of (b) J52:PAcT-Cl and (d) J52:CAcT-Cl films. (e) GIWAXS patterns of J52:PAcT-Cl and J52:CAcT-Cl films. (f) Out-of-plane and in-plane line-cut profiles of the binary blend films. (g) The peaks and corresponding CCL values in the IP and OOP direction of the blend films.

The morphologies of the pure and blend films were further investigated by atomic force microscopy (AFM) and high-resolution transmission electron microscopy (TEM). From the AFM image of the pure PAcT-Cl (Fig. S12), one can clearly see the fibril-like network surface with a root-mean-square (RMS) roughness value of 1.14 nm. While for the CAcT-Cl, the surface was replaced by the nodular gully, which increased the RMS to 1.2 nm. The fibril-like network morphology of PAcT-Cl indicates a better crystallinity and enhanced efficiency in OSCs. As shown in Fig. 5a and 5c, the J52:PAcT-Cl and J52:CAcT-Cl blend films displayed RMS roughness of 1.1 and 1.34 nm, respectively, indicating better miscibility between J52 and PAcT-Cl. What's more, surface patterns for J52:CAcT-Cl film showed a rough nodular character, indicative of a significantly large extent of phase separation. In contrast, a smoother surface morphology were observed for J52:PAcT-Cl film, which explains the observed higher performance arising from enhanced exciton diffusion/dissociation and charge carrier transport. Optimal crystalline domains and phase separation are beneficial to charge carrier transport and for achieving high FF in the related devices. From the AFM phase images in Fig. S13, J52:CAcT-Cl blend film exhibited more gully texture than that of J52:PAcT-Cl, suggesting the rough surface of the blend. The BHJ morphology was further visualized by TEM (Fig. 5b and 5d). Both blend films formed nanoscale phase separation and bi-continuous networks with a well-dispersed fibrillar structure. Though similar bright and dark regimes were observed both for J52:PAcT-Cl and J52:CAcT-Cl blend films, the J52:PAcT-Cl presented a more pronounced fibrillar network and distinct phase separation compared to the J52:CAcT-Cl films.

Grazing incidence wide-angle X-ray scattering (GIWAXS) was performed to investigate the molecular orientation and packing behaviors of the pure and blend films. As shown in Fig. S14a, the pristine PAcT-Cl exhibited obvious π–π stacking (d = 3.58 Å) peak at 1.75 Å^{-1} in the out-of-plane (OOP) direction and a (100) diffraction peak at 0.32 Å^{-1} in the in-plane (IP) direction, indicating a dominant face-on oriented molecular stacking, which is beneficial for vertical charge transport. In contrast, for CAcT-Cl, both distinct (100) diffraction peak at 0.43 Å^{-1} and week (010) diffraction peak at 1.72 Å^{-1} in the OOP direction were observed, implying the mixed face-on and edge on orientation (Fig. S14b). What's more, the crystalline coherence length (CCL) of PAcT-Cl in the IP direction was much larger than that of CAcT-Cl (CCL of 68.85 Å and 14.36 Å for PAcT-Cl and CAcT-Cl, respectively), indicating better molecular stacking and crystallinity for PAcT-Cl, which was consistent with the electron mobility and Raman tests. The 2D GIWAXS patterns and 1D line cuts of the BHJ films are shown in Fig. 5e-f and the detailed GIWAXS parameters are summarized in Table S5. Both J52:PAcT-Cl and J52:CAcT-Cl blend films preferred face-on orientations. Specifically, J52:PAcT-Cl blend film showed a larger CCL of 88.2 Å (Fig. 5g) in the IP direction than that of J52:CAcT-Cl (CCL of 49.96 Å), implying the enhanced crystallinity in lamellar stacking in the J52:PAcT-Cl film. Moreover, the π–π stacking distance for J52:PAcT-Cl (3.54 Å) in the OOP direction is smaller than that of J52:CAcT-Cl (3.56 Å), suggesting closer molecular stacking. J52:PAcT-Cl with better π–π stacking orientation helped improve charge transport and collection and thus yielded a high FF, which is in agreement with the higher charge carrier mobilities and better device performances. These results were in strong agreement with the suggestion that the PAcT-Cl exhibited better miscibility with J52 and can optimize the crystallinity and phase separation, which adversely impacted exciton dissociation and charge carrier transport efficiencies.

3. Conclusion

We have developed two simple non-fused ring electron acceptors by incorporating ethynylene as an linker, namely PAcT-Cl and CAcT-Cl. Compared to the CAcT-Cl containing 4H-cyclopenta[1,2-b:5,4-b']dithiophene core, PAcT-Cl with an alkoxy phenyl group core exhibited a downshifted HOMO level and improved face-on orientation. Consequently, OSCs processed by non-halogenated solvent *o*-xylene based on J52:PAcT-Cl showed a PCE of 10.22%, which is higher than that (7.32%) obtained from CAcT-Cl-based devices. We also investigated the OSCs performance processed by different halogenated solvents. Further study showed that J52:PAcT-Cl exhibited low charge recombination, higher charge mobility, superior ordered stacking and optimal blend morphology compared to J52:CAcT-Cl. Overall, our work proves that the ethynylene can be used to construct efficient NFREAs and also highlight the potential of non-halogenated solvent in preparing NFREAs-based devices.

Conflicts of interest

There are no conflicts to declare.

Acknowledgements

W. Y. W. thanks the RGC Senior Research Fellowship Scheme (SRFS2021-5S01), the Hong Kong Polytechnic University, Research Institute for Smart Energy (CDAQ) and Miss Clarea Au for the Endowed Professorship in Energy (847S). A. K. K. Kyaw thanks financial support from the Shenzhen Science, Technology and Innovation Commission (JCYJ20220530113014033) and the Guangdong Natural Science and Foundation.

Notes and references

[1] G. Zhang, F. R. Lin, F. Qi, T. Heumuller, A. Distler, H. J. Egelhaaf, N. Li, P. C. Y. Chow, C. J. Brabec, A. K. Jen and H. L. Yip, *Chem. Rev.*, 2022, **122**, 14180–14274.

[2] P. Cheng, G. Li, X. Zhan and Y. Yang, *Nat. Photonics*, 2018, **12**, 131–142.

[3] J. Zhang, H. S. Tan, X. Guo, A. Facchetti and H. Yan, *Nat. Energy*, 2018, **3**, 720–731.

[4] D. Luo, W. Jang, D. Babu, M. S. Kim, D. H. Wang and A. K. K. Kyaw, *J. Mater. Chem. A*, 2022, **10**, 3255–3295.

[5] L. Zhu, M. Zhang, J. Xu, C. Li, J. Yan, G. Zhou, W. Zhong, T. Hao, J. Song, X. Xue, Z. Zhou, R. Zeng, H. Zhu, C. C. Chen, R. C. I. MacKenzie, Y. Zou, J. Nelson, Y. Zhang, Y. Sun and F. Liu, *Nat. Mater.*, 2022, **21**, 656–663.

[6] Z. Chen, H. Yao, J. Wang, J. Zhang, T. Zhang, Z. Li, J. Qiao, S. Xiu, X. Hao and J. Hou, *Energy Environ. Sci.*, 2023, **16**, 2637–2645.

[7] J. Yuan, Y. Zhang, L. Zhou, G. Zhang, H.-L. Yip, T.-K. Lau, X. Lu, C. Zhu, H. Peng, P. A. Johnson, M. Leclerc, Y. Cao, J. Ulanski, Y. Li and Y. Zou, *Joule*, 2019, **3**, 1140–1151.

[8] J. Zhang, H. Mao, K. Zhou, L. Zhang, D. Luo, P. Wang, L. Ye and Y. Chen, *Adv. Mater.*, 2024, **36**, 2309379.

[9] L. Wen, H. Mao, L. Zhang, J. Zhang, Z. Qin, L. Tan and Y. Chen, *Adv. Mater.*, 2024, **36**, 2308159.

[10] X. Yu, P. Ding, D. Yang, P. Yan, H. Wang, S. Yang, J. Wu, Z. Wang, H. Sun, Z. Chen, L. Xie,

and Z. Ge, *Angew. Chem. Int. Ed.*, 2024, e202401518.

[11] J. Zhou, D. Li, L. Wang, X. Zhang, N, Deng, C. Guo, C. Chen, Z. Gan, C. Liu, W. Sun, D. Liu, W. Li, Z. Li, K. Wang and T. Wang, *Interdiscip. Mater.*, 2023, **2**, 866–875.

[12] L. Wang, C. Chen, Y. Fu, C. Guo, D. Li, J. Cheng, W. Sun, Z. Gan, Y. Sun, B. Zhou, C. Liu, D. Liu, W. Li and T. Wang, *Nat. Energy*, 2024, **9**, 208–218.

[13] C. Liu, Y. Fu, J. Zhou, L. Wang, C. Guo, J. Cheng, W. Sun, C. Chen, J. Zhou, D. Liu, W. Li, and T. Wang, *Adv. Mater.*, 2024, **36**, 2308608.

[14] D. Luo, C. J. Brabec and A. K. K. Kyaw, *Nano Energy*, 2023, **114**, 108661.

[15] J. Min, Y. N. Luponosov, C. Cui, B. Kan, H. Chen, X. Wan, Y. Chen, S. A. Ponomarenko, Y. Li and C. J. Brabec, *Adv. Energy Mater.*, 2017, **7**, 1700465.

[16] H. Gao, C. Han, X. Wan and Y. Chen, *Ind. Chem. Mater.*, 2023, **1**, 60–78.

[17] A. Mishra and G. D. Sharma, *Angew. Chem. Int. Ed.*, 2023, **62**, e202219245.

[18] D. Luo, X. Lai, N. Zheng, C. Duan, Z. Wang, K. Wang and A. K. K. Kyaw, *Chem. Eng. J.*, 2021, **420**, 129768.

[19] L. Ma, S. Zhang, J. Zhu, J. Wang, J. Ren, J. Zhang and J. Hou, *Nat. Commun.*, 2021, **12**, 5093.

[20] X. Wang, H. Lu, Y. Liu, A. Zhang, N. Yu, H. Wang, S. Li, Y. Zhou, X. Xu, Z. Tang and Z. Bo, *Adv. Energy Mater.*, 2021, **11**, 2102591.

[21] D. L. Ma, Q. Q. Zhang and C. Z. Li, *Angew. Chem. Int. Ed.*, 2023, **62**, e202214931.

[22] D. Li, H. Zhang, X. Cui, Y. N. Chen, N. Wei, G. Ran, H. Lu, S. Chen, W. Zhang, C. Li, Y. Liu, Y. Liu and Z. Bo, *Adv. Mater.*, 2024, **36**, 2310362.

[23] Q. Zhang, X. Xu, S. Chen, G. B. Bodedla, M. Sun, Q. Hu, Q. Peng, B. Huang, H. Ke, F. Liu, T. P. Russell and X. Zhu, *Sustainable Energy Fuels*, 2018, **2**, 2616.

[24] D. Luo, L. Li, Y. Shi, J. Zhang, K. Wang, X. Guo and A. K. K. Kyaw, *J. Mater. Chem. A*, 2021, **9**, 14948–14957.

[25] D. Luo, Z. Jiang, C. Shan, L. Li, C. Duan, Q. Liu, Z. Wang, K. Wang, B. Xu and A. K. K. Kyaw, *ACS Appl. Mater. Interfaces*, 2022, **14**, 24374–24385.

[26] D. Luo, Z. Jiang, W. Yang, X. Guo, X. Li, E. Zhou, G. Li, L. Li, C. Duan, C. Shan, Z. Wang, Y. Li, B. Xu and A. K. K. Kyaw, *Nano Energy*, 2022, **98**, 107186.

[27] D. Luo, L. Zhang, J. Zeng, W. Chi, J. Zhou, E. Zhou, L. Li, T. Iwahashi, T. Michinobu, Y.

Ouchi, B. Xu and A. K. K. Kyaw, *Adv. Funct. Mater.*, 2023, 202311736.

[28] C. Yang, M. Jiang, S. Wang, B. Zhang, P. Mao, H. Y. Woo, F. Zhang, J.-L. Wang and Q. An, *Adv. Mater.*, 2024, **36**, 2305356.

[29] S. Luo, C. Li, J. Zhang, X. Zou, H. Zhao, K. Ding, H. Huang, J. Song, J. Yi, H. Yu, K. S. Wong, G. Zhang, H. Ade, W. Ma, H. Hu, Y. Sun and H. Yan, *Nat. Commun.*, 2023, **14**, 6964.

[30] D. Wang, G. Zhou, Y. Li, K. Yan, L. Zhan, H. Zhu, X. Lu, H. Chen and C. Z. Li, *Adv. Funct. Mater.*, 2022, **32**, 2107827.

[31] Z. Gan, L. Wang, J. Cai, C. Guo, C. Chen, D. Li, Y. Fu, B. Zhou, Y. Sun, C. Liu, J. Zhou, D. Liu, W. Li, and T. Wang, *Nat. Commun.*, 2023, **14**, 6297.

[32] N. Yoon, J.-Y. Jeong, S. Oh, C. E. Song, H. K. Lee, W. S. Shin, J.-C. Lee, S.-J. Moon and S. K. Lee, *ACS Appl. Energy Mater.*, 2020, **3**, 12327–12337.

[33] S. Li, L. Zhan, W. Zhao, S. Zhang, B. Ali, Z. Fu, T.-K. Lau, X. Lu, M. Shi, C.-Z. Li, J. Hou and H. Chen, *J. Mater. Chem. A*, 2018, **6**, 12132–12141.

[34] F. G. Guijarro, P. Cruz, K. Khandelwal, R. Singhal, F. Langa and G. D. Sharma, *ACS Appl. Mater. Interfaces* 2023, **15**, 21296–21305.

[35] A. K. K. Kyaw, D. H. Wang, V. Gupta, W. L. Leong, L. Ke, G. C. Bazan, and A. J. Heeger, *ACS Nano*, 2013, **7**, 4569–4577.

[36] A. K. Kyaw, D. H. Wang, D. Wynands, J. Zhang, T. Q. Nguyen, G. C. Bazan and A. J. Heeger, *Nano Lett.*, 2013, **13**, 3796–3801.

[37] Y. Zhang, D. Luo, C. Shan, Q. Liu, X. Gu, W. Li, W. C. H. Choy and A. K. K. Kyaw, *Solar RRL*, 2021, **6**, 2100785.

[38] J. Zhou, D. He, Y. Li, F. Huang, J. Zhang, C. Zhang, Y. Yuan, Y. Lin, C. Wang and F. Zhao, *Adv. Mater.*, 2022, **35**, 2207336.

[39] C. G. Shuttle, B. O’Regan, A. M. Ballantyne, J. Nelson, D. D. C. Bradley, J. de Mello and J. R. Durrant, *Appl. Phys. Lett.*, 2008, **92**, 093311.

[40] B. Fan, W. Gao, R. Zhang, W. Kaminsky, F. R. Lin, X. Xia, Q. Fan, Y. Li, Y. An, Y. Wu, M. Liu, X. Lu, W. J. Li, H.-L. Yip, F. Gao and A. K. Y. Jen, *J. Am. Chem. Soc.*, 2023, **145**, 5909–5919.

[41] D. Luo, Z. Jiang, W. L. Tan, L. Zhang, L. Li, C. Shan, C. R. McNeill, P. Sonar, B. Xu and A. K. K. Kyaw, *Adv. Energy Mater.*, 2022, **13**, 2203402.

[42] D. Luo, L. Li, E. Zhou, W.-Y. Wong and A. K. K. Kyaw, *Mater. Adv.*, 2023, **4**, 4444–4454.

[43] D. Luo, Y. Zhang, L. Li, C. Shan, Q. Liu, Z. Wang, W. C. H. Choy and A. K. K. Kyaw, *Mater. Today Energy*, 2022, **24**, 100938.

[44] S. Nilsson, A. Bernasik, A. Budkowski and E. Moons, *Macromolecules*, 2007, **40**, 8291–8301.